# Nanoscale
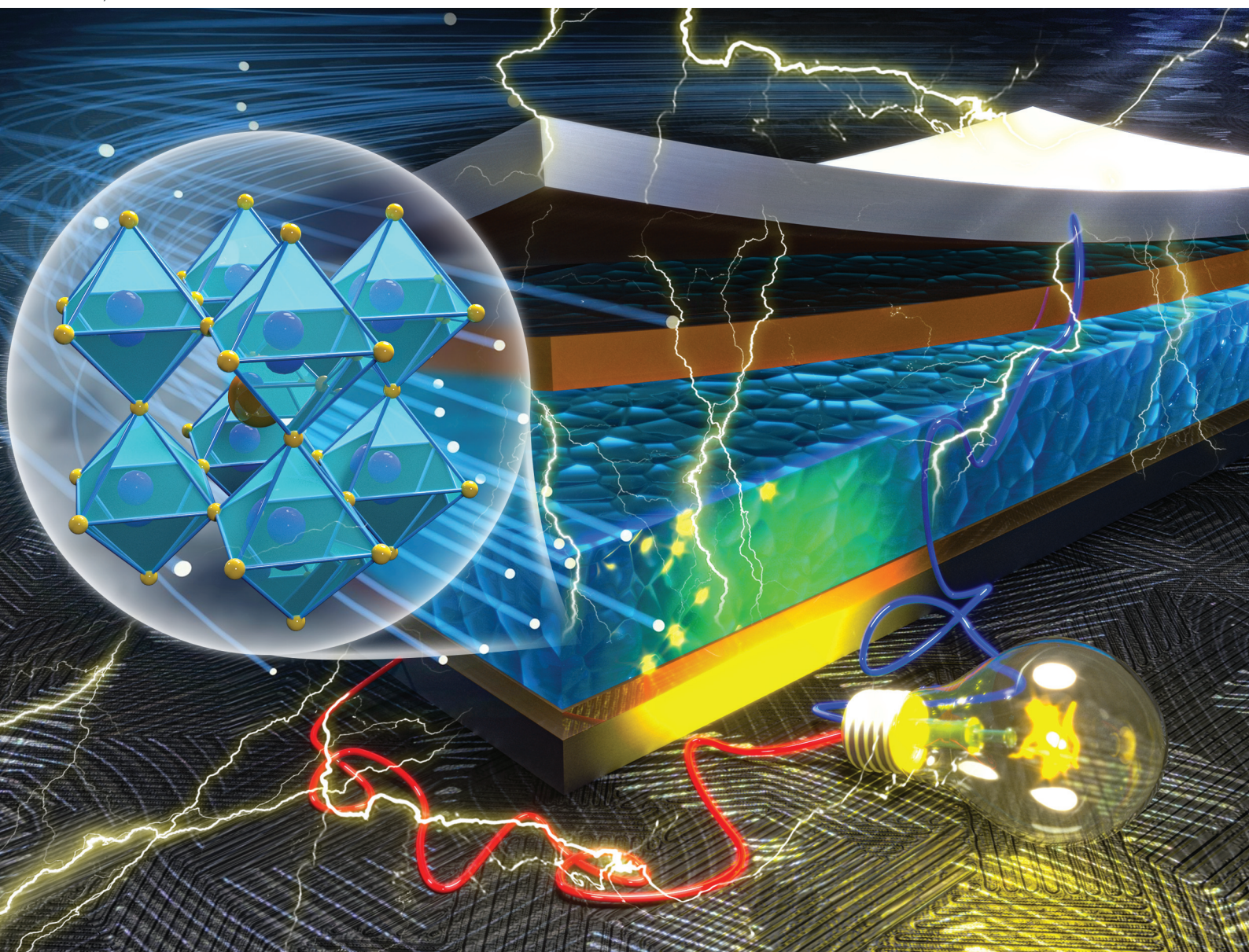
ROYAL SOCIETY
OF CHEMISTRY

**PAPER**
Shengjun Li *et al.*
Enhancing the performance of n-i-p perovskite solar cells by
introducing hydroxyethylpiperazine ethane sulfonic acid for
interfacial adjustment

NCNST

## PAPER

Check for updates

# Enhancing the performance of n-i-p perovskite solar cells by introducing hydroxyethylpiperazine ethane sulfonic acid for interfacial adjustment†

Putao Zhang, (ID) Yiming Chen, Shenghan Wu, Xiaohui Li, Meiyue Liu and Shengjun Li*

Although the power conversion efficiency (PCE) of perovskite solar cells (PSCs) has improved greatly in recent years, the challenges of efficiency and stability still need to be overcome before these solar cells can be used in commercial applications. Here, a weak acid buffer, hydroxyethyl piperazine ethane sulfonic acid (HEPES), is used to passivate the interface of an $SnO_2$ electron transport layer (ETL) and a photoactive layer in n-i-p solar cells. The device efficiency based on a $SnO_2$/HEPES ETL reaches 20.22%, which is 9.7% higher than that of the control (18.43%), and the device stability is also significantly improved. The improvement in the device performance is mainly due to the introduction of the HEPES interface layer to adjust the interface energy level, which also improves the crystallinity of the perovskite film and reduces the interface defects. Electrochemical impedance spectroscopy and transient photovoltage/photocurrent results show that the HEPES-modified PSCs have lower charge transfer resistance, weaker leakage current intensity and improved interfacial charge separation and transport.

## Introduction

Over the past two decades, organic–inorganic hybrid perovskite solar cells (PSCs) have become one of the research hotspots in the field of photovoltaics, because of their simple preparation process and high efficiency. In the short period of more than 10 years, the power conversion efficiency (PCE) of PSCs has rapidly been improved from 3.8% to 25.6% (certified 25.5%).[1,2] The high efficiency of solar cells is mainly due to the excellent photoelectric properties, of the perovskite photoactive materials (such as $CH_3NH_3PbX_3$, X = I, Br, Cl), such as strong absorption coefficient,[3,4] high carrier mobility,[5] long carrier lifetime,[6] and tunable direct band gaps.[7,8] However, although the efficiency has been significantly improved, the serious hysteresis and poor stability of PSCs limit their further commercial applications.

As the electron transport material in n-i-p PSCs, the $SnO_2$ ETL has the advantages of high electron mobility, high light transmittance, and it can be prepared at a low temperature because of the large band gap.[9–11] However, due to the mismatch of energy levels and the existence of defects,[12–14] the efficiency of charge extraction at the $SnO_2$/perovskite interface

is low, and the carrier recombination is serious, which leads to low efficiency and poor stability of the device. In order to solve these problems, researchers have proposed some ETL modification methods: (1) by doping the metal ions, the ETL can better match the energy level of the perovskite materials and also improve the conductivity of the ETL,[15,16] and previous studies have shown that the MgO doped $SnO_2$ film is uniform and dense, which can effectively improve the carrier mobility;[17] (2) by adding an interface modification layer, the surface defect state is passivated to improve the carriers' transport and separation at the interface.[9,18,19] Fullerene and its derivatives have a good electron extraction ability, and their energy levels match well with those of perovskite. It is reported that fullerene modified $SnO_2$ shows good electron transfer and negligible charge recombination.[9,20–22] These studies improve the device performance by reducing the ETL surface defects or improving the energy level alignment. The ETL and perovskite active layer are the key components of perovskite solar cells. The development of an interface modification layer can not only improve the performance of ETL, but it can also have a positive impact on perovskite crystallization, which will be very helpful for improving the overall performance of the device.

Here, a multifunctional molecule is introduced: hydroxyethylpiperazine ethane sulfonic acid (HEPES), with a sulfonic group and a hydroxyethyl group, on the surface of the $SnO_2$ ETL to passivate the $SnO_2$ surface defects, improve the interface environment of the $SnO_2$/perovskite, optimize the crystal-

*Key Laboratory of Photovoltaic Materials, Henan University, Henan, Kaifeng 475004, China. E-mail: lishengjun@henu.edu.cn*

lization process of the perovskite, and to improve the quality of the perovskite films. Compared with $SnO_2$ ETL, the HEPES modified $SnO_2$ film is less rough and is a better match with the perovskite energy level. Compared with the control, the perovskite deposited on $SnO_2$/HEPES substrate has large and dense grains and a more effective carrier extraction. The efficiency of the $SnO_2$/HEPES based solar cell reaches 20.22%, with a significantly reduced hysteresis, and the long-term stability is also improved.

## Results and discussion

Fig. 1a shows the molecular structure model of HEPES, which contains a hydroxyl (–OH), two nitrogen atoms (N) and a sulfonic group (–$HSO_3$). The abundant functional groups make HEPES a candidate material for $SnO_2$ surface passivation. On the one hand, –OH can react with the surface groups (such as carboxyl) of $SnO_2$, thus blocking the polar groups of $SnO_2$. Fig. S1 (ESI†) shows the Fourier-transform infrared (FTIR) spectrum of fresh $SnO_2$ film after plasma treatment, and it can be seen from the FTIR results that there are absorption peaks in the range of 1580–1644 $cm^{-1}$ and at 1731 $cm^{-1}$, which belong to the absorption peaks of the carboxyl group.[23] On the other hand, the –$HSO_3$ and N atoms form Lewis adducts with negative/positive charge trap states, which passivate the defects on the surface of the perovskite. Density functional theory (DFT) was used to determine the surface electrostatic potential of HEPES. As shown in Fig. 1b, the –$HSO_3$ and –OH groups are located in the negative and positive electrostatic potential regions, respectively, and these can participate in the coordination or bonding of uncoordinated $Pb^{2+}$ or halogen defects in the perovskite. It can be seen from the electrostatic potential distribution diagram of the HEPES molecule that –$HSO_3$ is located in the blue region, that is, it belongs to the electron-deficient group. Electron-deficient groups are easy to interact with electron-rich groups. From the DFT calculation, it was further determined that the most easily formed defect in perovskite is the lead iodine substitutions defect ($Pb_I$), and its formation energy is 0.43 eV. The formation energies of the Pb vacancy defects and I vacancy defects are 7.27 and 36.24 eV, respectively. $Pb_I$ defects could easily form and contains many electrons, which act as a lewis acid to coordinate with the existed –$HSO_3$. The interaction between $Pb_I$ and –$HSO_3$ is beneficial to promote the formation of large grains with small defects.[24]

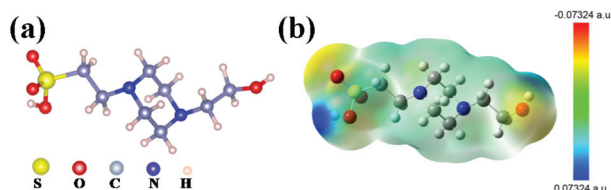The FTIR spectroscopy was performed to determine the binding between $SnO_2$ and HEPES. As shown in Fig. S2 (ESI†), the FTIR spectra for HEPES have a strong peak at 3386 $cm^{-1}$, which is the characteristic peak of the O–H bond. In Fig. 2a, the peak at 1672 $cm^{-1}$ is assigned to the stretching vibration of the C=O bond. When the $SnO_2$ combines with HEPES, the peak value of C=O shifts to a lower wavenumber of 1664 $cm^{-1}$, which indicates that the $SnO_2$ mainly interacts with the –OH on HEPES. This confirmed that HEPES was chemically anchored on the $SnO_2$ surface. In order to further understand the difference of the optical properties between the ETL films before and after passivation, the optical transmission spectra of the two films were measured, as shown in Fig. 2b. According to reports in the literature, $SnO_2$ nanocrystalline thin films prepared at low temperature have good transmittance due to their excellent anti-reflection ability.[25] Interestingly, in the visible region (400–800 nm), both $SnO_2$ and $SnO_2$/HEPES films show good light transmittance. Because the HEPES passivation layer is very thin, the light transmittance of the film does not decrease after the introduction of HEPES, which is conducive to photons reaching the perovskite layer. The water contact angles of $SnO_2$ and $SnO_2$/HEPES films were determined. The results of this are shown in Fig. 2c and d, and the contact angle of the $SnO_2$ film is 14.6° (the average contact angle is 13.56°, see Fig. S3, ESI†). Whereas, the contact angle of the $SnO_2$ substrate coated by HEPES is 11.9° (average is 10.68°), and the hydrophilicity is stronger. Because HEPES has good hydrophilicity, the interface modification with HEPES can cause the perovskite precursor and ETL substrate to infiltrate well, which is beneficial for reducing the Gibbs free energy of the perovskite crystallization and improving the quality of perovskite crystallization.[14,26]

Scanning electron microscopy (SEM) and atomic force microscopy (AFM) were used to further characterize the surface morphology of the substrate before and after passivation. The results are shown in Fig. 3. The SEM images show that the $SnO_2$ nanocrystals are densely arranged and comple-
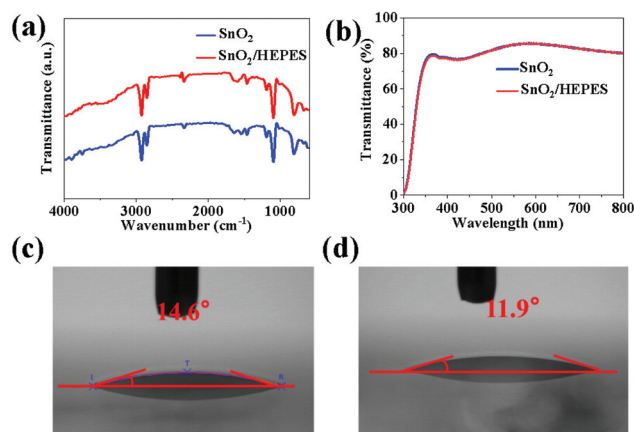
**Fig. 2** (a) Fourier transform infrared spectra, (b) UV-Vis transmittance spectra of $SnO_2$ and $SnO_2$/HEPES films. Water contact angles of $SnO_2$ (c) and $SnO_2$/HEPES (d) substrates.
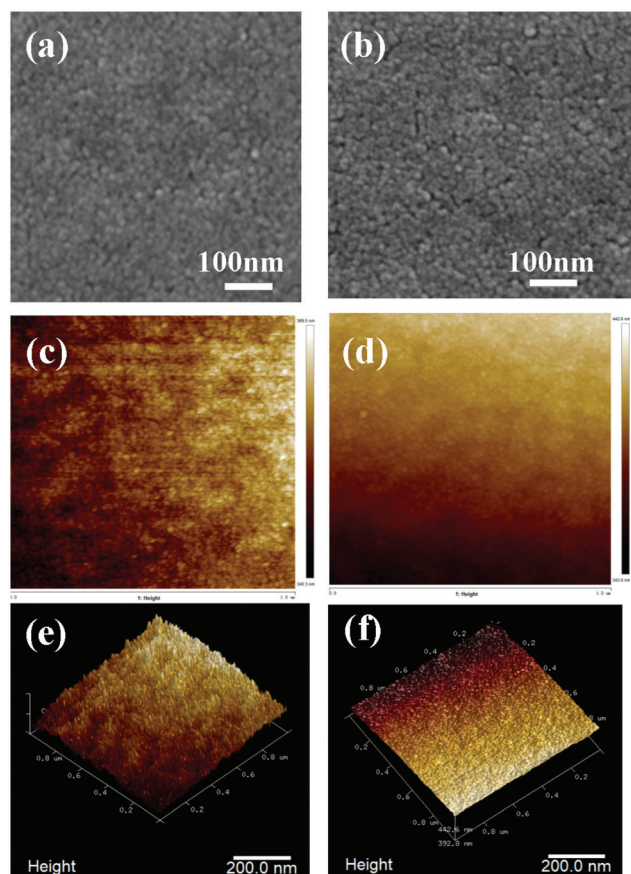
**Fig. 1** (a) Molecular model of HEPES. (b) Electrostatic potential profile of HEPES.

**Fig. 3** Top-view scanning electron microscopy images of $SnO_2$ layers without (a), and with (b) HEPES. Atomic force microscopy images of $SnO_2$ without (c and e), and with (d and f) HEPES.



**Fig. 4** The SEM images of the perovskite film deposited on $SnO_2$ (a), and on $SnO_2$/HEPES (b) substrate. (c) The XRD, and (d) UV-Vis patterns for perovskite films on different substrates.

tely covered the ITO surface (Fig. 3a). Due to the thin passivation layer of HEPES, there is almost no obvious effect on the morphology of the substrate after covering the $SnO_2$ surface (Fig. 3b). The 2D and 3D AFM images (Fig. 3c–f) show that the surface roughness of the $SnO_2$/HEPES film is 1.23 nm, which is lower than the 1.57 nm on a bare $SnO_2$ substrate. This result shows that HEPES is beneficial to the growth of the perovskite crystal.[27]

The perovskite thin films were prepared on $SnO_2$ and $SnO_2$/HEPES ETL using a one-step anti-solvent method. The morphology of the perovskite films was studied by FE-SEM. In Fig. 4a and b, the perovskite crystal on the $SnO_2$/HEPES substrate is more uniform and denser than that on the $SnO_2$ substrate, and the grain size is also increased. The statistical results of the grain size are shown in Fig. S4 (ESI†). The average size of perovskite crystal on $SnO_2$/HEPES substrate reached 310 nm, which is higher than the 190 nm on the control. The effect of the substrate on the crystal structure of perovskite was determined by X-ray diffraction (XRD). As shown in Fig. 4c, the XRD patterns of perovskite films on $SnO_2$ and $SnO_2$/HEPES substrates show peaks of 14.1° (110), 28.4° (220) and 31.9° (310), which can be indexed as a methylammonium lead triiodide $(MAPbI_3)$ tetragonal crystal
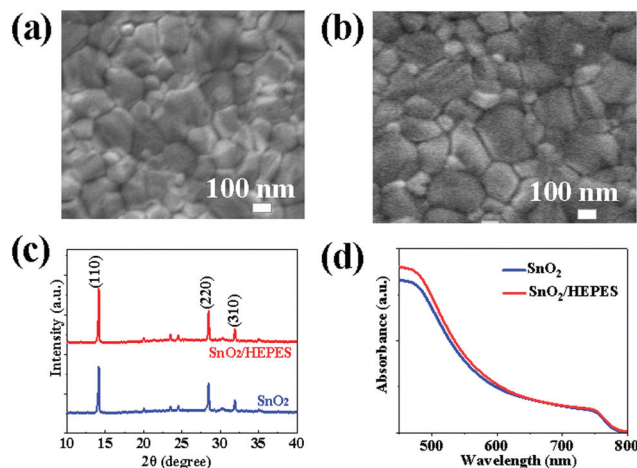
structure.[28,29] Compared with the crystal deposited on the $SnO_2$ substrate, the crystal grown on the $SnO_2$/HEPES substrate has a higher crystal strength and a smaller full width at half maximum (FWHM) (Fig. S5, ESI†), which indicates that the crystallinity of $MAPbI_3$ on $SnO_2$/HEPES is better. The UV-Vis absorption spectrum of the perovskite film is shown in Fig. 4d. The results show that the perovskite films with an $SnO_2$/HEPES underlayer have a higher absorption in the visible range, which is mainly due to the better crystallinity and smoother surface.[30] Subsequently, the electron-only devices with a structure of ITO/ETL/perovskite/PCBM/Ag (Fig. 5a) was adopted for space-charge-limited current (SCLC) measurements to test the defect density of the $MAPbI_3$ films deposited on different ETL substrates.[31] The $J$–$V$ curves tested in the dark state are shown in Fig. 5b and c, which includes the ohmic region (linear current–voltage response) at a low bias voltage range and a trap-filling limited region as the current increased significantly. Eqn (1) is used to calculate the trap density $(N_t)$:[32,33]

$$N_t = \frac{2V_{TFL}\varepsilon_r\varepsilon_0}{qL^2} \qquad (1)$$

where $L$, $\varepsilon_0$, $\varepsilon_r$, and $q$ represent the $MAPbI_3$ thickness, vacuum permittivity, dielectric constant of $MAPbI_3$ and electron
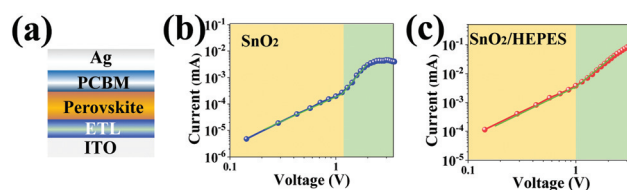


**Fig. 5** (a) A schematic diagram of electron-only devices with a structure of ITO/ETL/perovskite/PCBM/Ag. (b) and (c) Space-charge-limited current *versus* voltage of $SnO_2$ and $SnO_2$/HEPES based devices, respectively.

charge, respectively. The values of $N_t$ calculated from the curve of $SnO_2$ and $SnO_2$/HEPES samples are $2.77 \times 10^{14}$ cm$^{-3}$, and $2.49 \times 10^{14}$ cm$^{-3}$, respectively. The results show that the HEPES surface modification is helpful for improving the quality of perovskite films and reducing the perovskite defects, which is consistent with the XRD and SEM measurements.

Steady state photoluminescence (PL) and time-resolved photoluminescence (TRPL) were measured to investigate the effect of the HEPES interface layer on the charge extraction and electron transport behavior. As shown in Fig. 6a, the PL intensity of the perovskite film grown on $SnO_2$/HEPES substrate is significantly weaker than that grown on bare $SnO_2$, which indicated that MAPbI$_3$ film grown on $SnO_2$/HEPES substrate exhibits more effective PL quenching than that on the $SnO_2$ substrate. The rapid quenching of the PL indicates that the interface layer of HEPES makes the carrier transport between perovskite and ETL more efficient. Fig. 6b shows the TRPL spectra of perovskite films on $SnO_2$ and $SnO_2$/HEPES substrates. The bi-exponential function eqn (2) is used to fit the PL decay curves.[34,35] The fitting parameters are summarized in Table S1 (ESI†).

$$I(t) = A_1 \exp\left(-\frac{t}{\tau_1}\right) + A_2 \exp\left(-\frac{t}{\tau_2}\right) + A_0 \qquad (2)$$

where $A_0$ is a constant, $A_1$ and $A_2$ represent the PL decay amplitudes, $\tau$ is a decay time constant. The fast decay lifetime ($\tau_1$) and the slow decay lifetime ($\tau_2$) indicate the PL quenching at charge transfer on the ETL/perovskite interface, and the radiative recombination of trapped charges within the perovskite layers, respectively.[14,36] It was found that perovskite films deposited on $SnO_2$/HEPES have a shorter, fast decay time ($\tau_1$ = 7.86 ns) than that deposited on $SnO_2$ ($\tau_1$ = 11.93 ns), which indicates the fast charge extraction and reduced charge recombination for the HEPES treated samples. Meanwhile a longer, slow decay is observed for the $SnO_2$/HEPES/perovskite ($\tau_2$ = 46.12 ns), which demonstrates that the trap density in perovskite is reduced, and thus, the quality of the perovskite films is improved. This is consistent with the SEM and PL results. It is worth noting that the morphology and crystallinity results have proved that the introduction of HEPES can improve the crystallinity of the perovskite crystals and reduce the defects in the perovskite films. Thus, the accumulation of interfacial photoelectrons is reduced.
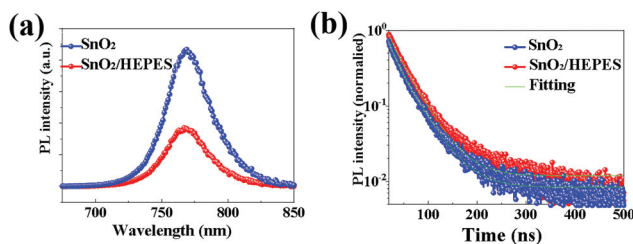


Fig. 6 Photoluminescence spectra (a), and time-resolved photoluminescence curves (b) of perovskite film based on different ETLs.

Perovskite solar cells with the structure ITO/ETL/MAPbI$_3$/Spiro-OMeTDA/Ag were prepared using $SnO_2$ and $SnO_2$/HEPES as electron transport layers. The device structure and energy level arrangement of each functional layer as shown in Fig. 7a and b. The SEM image of the cross section of the cell is shown in Fig. 7c, the thickness of the perovskite active layer is about 550 nm. The photovoltaic performance of the cells was measured under one standard simulated sunlight (AM1.5, 100 mW cm$^{-2}$). Fig. 7d shows the J–V curves of the control and HEPES modified cells. The detailed parameters are listed in Table S2 (ESI†). The PCE of the control reached 18.43% with an open circuit voltage ($V_{OC}$) of 1.06 V, a short circuit current density ($J_{SC}$) of 22.57 mA cm$^{-2}$, and a fill factor (FF) of 76.69%. While $J_{SC}$ and PCE increased to 23.59 mA cm$^{-2}$ and 20.22%, respectively, for HEPES modified best device. Fig. 7e shows the incident-photon-to-current-efficiency (IPCE) curve of monochromatic light incidence. The integrated current of the HEPES modified cells increased from 21.69 to 23.01 mA cm$^{-2}$. This shows the superiority of the charge injection and collection of the HEPES modified devices. In order to further study the effect of the HEPES interface layer on the performance of the solar cell, the J–V curves of the cell in the dark were measured. As shown in Fig. S6 (ESI†), the dark current density of the HEPES modified device is lower than that of the control device, which indicates that the current leakage phenomenon is effectively suppressed after the interface modification. This is consistent with the measurement results of the steady-state PL and TRPL. It further shows that the surface modification layer of HEPES obviously reduced the charge recombination. Next the electrochemical impedance spectroscopy (EIS) of the operational $SnO_2$ and $SnO_2$/HEPES based perovskite solar cells were measured under dark conditions and the Nyquist plots (bias = 0.8 V) are shown in Fig. 7f. For the two devices, we applied an equivalent circuit model to fit the series resistance ($R_s$) and recombination resistance ($R_{rec}$) and the fitting parameters are summarized in Table S3 (ESI†), and the equivalent circuit model is shown in the inset of Fig. 7f. Based on the fitting results, the $R_s$ was found to decrease from 43 Ω (for the $SnO_2$-based device) to 32 Ω (for the $SnO_2$/HEPES device), which is consistent with the improved electron extraction at the cathode interface. The $R_{rec}$ increases from 733 Ω (for the $SnO_2$-based device) to 1053 Ω (for the $SnO_2$/HEPES device), indicating the effectively suppressed carrier recombination in the perovskite solar cells with the inserted HEPES layer.

Long-term stability is another key indicator to evaluate the performance of the perovskite solar cells. The long-term stability of perovskite solar cells stored under ambient conditions without encapsulation is tested further. As shown in Fig. S7 (ESI†), for the normalized PCE decay versus storage time, 86% of the initial PCE is maintained for the $SnO_2$/HEPES based sample after 30 d of storage in an ambient environment ($T \approx 25$ °C, RH $\approx 50$%), whereas the control device only retains 74% of the initial efficiency after one month. Considering the improvement of film quality, in particular for the compact perovskite with large grains for the $SnO_2$/HEPES sample, the probability of water molecules diffusing into the internal region of
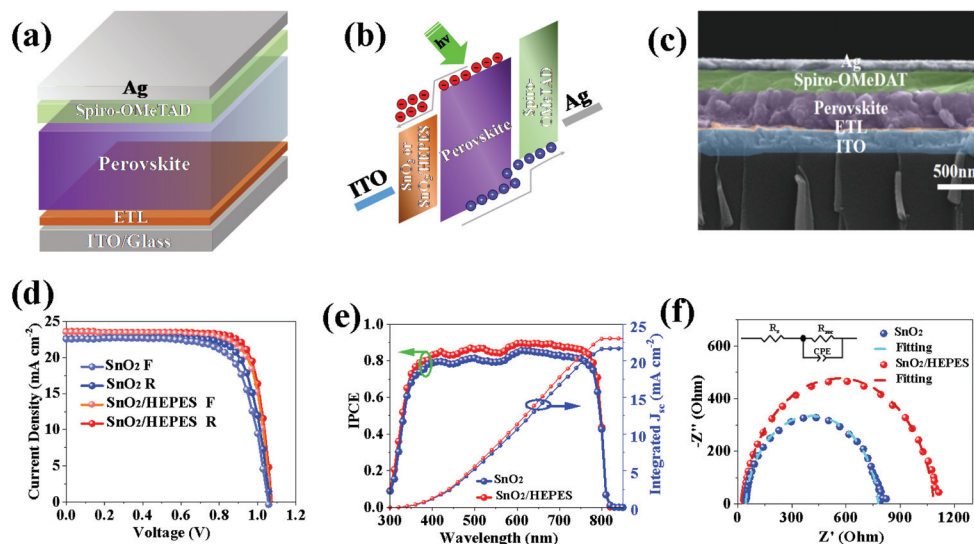
**Fig. 7** (a) Device structure of the p-i-n PSCs, (b) corresponding energy-level diagram of the structure shown in (a), (c) cross-sectional SEM image of the device, (d) the $J-V$ curves of the best PSCs under reverse and forward scans, (e) the IPCE spectra, and integrated $J_{sc}$ of the corresponding devices, and (f) the Nyquist plot of the impedance spectroscopy of $SnO_2$ and $SnO_2$/HEPES based perovskite solar cells measured in the dark at 0.6 V, together with the fitting results with an equivalent circuit model (inset).

the perovskite film will be reduced. Therefore, under the same environment ($T \approx 25$ °C, RH $\approx 50\%$), the decomposition of perovskite deposited on $SnO_2$/HEPES is minimized, and finally the stability of the device is improved.

The transient photocurrent (TPC) decay and transient photovoltage (TPV) decay are important means to study the charge transfer performance of the solar cell devices. As Fig. 8a shows, compared to the $SnO_2$-based sample, the $SnO_2$/HEPES based device gave a reduced TPC response, showing that charge extraction and transmission is more effective than that in the control device. In Fig. 8b, the TPV response of the $SnO_2$/HEPES sample exhibits a longer lifetime than that of the control solar cell, which proves that carrier recombination is effectively suppressed in the $SnO_2$/HEPES based device.[37] The charge transport characteristics show that HEPES effectively passivates the ETL/perovskite interface, promotes the formation of high-quality perovskite, reduces the perovskite defect density, and promotes the carrier transport of the device, which enhances the PCE of the PSCs.

## Conclusions

In conclusion, HEPES is used to passivate the surface of the $SnO_2$ film. The results show that high quality perovskite thin films with improved crystallinity are obtained on the $SnO_2$/HEPES substrates. In addition, HEPES can passivate $SnO_2$ surface defects and improve the efficiency of the electron transport. The results showed that the PCE of HEPES modified PSCs was up to 20.22%. The improvement of device performance is mainly due to the introduction of the HEPES interface layer to adjust the interface energy level, improve the crystallinity of the perovskite film and reduce the interface defects. The EIS and TPV/TPC results further indicate that the HEPES modified PSCs have a lower carrier transfer resistance, lower leakage current density, and lower interface charge accumulation.

## Conflicts of interest

There are no conflicts to declare.

## Acknowledgements

## Notes and references

1 A. Kojima, K. Teshima, Y. Shirai and T. Miyasaka, Organometal halide perovskites as visible-light sensitizers
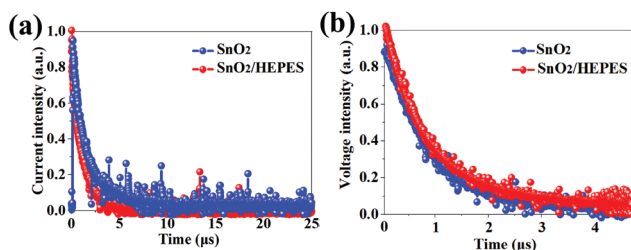


**Fig. 8** Normalized transient photocurrent (a), and transient optical-voltage (b) for PSCs without and with a HEPES layer.

for photovoltaic cells, *J. Am. Chem. Soc.*, 2009, **131**, 6050–6051.

2  J. Jeong, M. Kim, J. Seo, H. Z. Lu, P. Ahlawat, A. Mishra, Y. G. Yang, M. A. Hope, F. T. Eickemeyer, M. Kim, Y. J. Yoon, I. W. Choi, B. P. Darwich, S. J. Choi, Y. Jo, J. H. Lee, B. Walker, S. M. Zakeeruddin, L. Emsley, U. Rothlisberger, A. Hagfeldt, D. S. Kim, M. Grätzel and J. Y. Kim, Pseudo-halide anion engineering for α-FAPbI$_3$ perovskite solar cells, *Nature*, 2021, **59**, 2381.

3  E. T. Hoke, D. J. Slotcavage, E. R. Dohner, A. R. Bowring, H. I. Karunadasa and M. McGehee, Reversible photo-induced trap formation in mixed-halide hybrid perovskites for photovoltaics, *Chem. Sci.*, 2015, **6**, 613–617.

4  S.-H. Jeong, J. Park, T.-H. Han, F. Zhang, K. Zhu, J. S. Kim, M.-H. Park, M. O. Reese, S. Yoo and T.-W. Lee, Characterizing the efficiency of perovskite solar cells and light-emitting diodes, *Joule*, 2020, **4**, 1206–1235.

5  T. Matsushima, S. Hwang, A. S. Sandanayaka, C. Qin, S. Terakawa, T. Fujihara, M. Yahiro and C. Adachi, Solution–processed organic-inorganic perovskite field-effect transistors with high hole mobilities, *Adv. Mater.*, 2016, **28**, 10275–10281.

6  Q. Dong, Y. Fang, Y. Shao, P. Mulligan, J. Qiu, L. Cao and J. Huang, Electron-hole diffusion lengths >175 μm in solution-grown CH$_3$NH$_3$PbI$_3$ single crystals, *Science*, 2015, **347**, 967–970.

7  A. Perulli, A. Balena, M. Fernandez, G. Nedelcu, A. Cretí, M. V. Kovalenko, M. Lomascolo and M. Anni, Full-color tuning in binary polymer: perovskite nanocrystals organic-inorganic hybrid blends, *Appl. Phys. Lett.*, 2018, **112**, 171904.

8  N. Zibouche and M. Islam, Structure-electronic property relationships of 2D ruddlesden-popper tin-and lead-based iodide perovskites, *ACS Appl. Mater. Interfaces*, 2020, **12**, 15328–15337.

9  J. Wang, K. Datta, C. H. Weijtens, M. M. Wienk and R. A. Janssen, Insights into fullerene passivation of SnO$_2$ electron transport layers in perovskite solar cells, *Adv. Funct. Mater.*, 2019, **29**, 1905883.

10  Y. Lee, S. Lee, G. Seo, S. Paek, K. T. Cho, A. J. Huckaba, M. Calizzi, D. W. Choi, J. S. Park and D. J. Lee, Efficient planar perovskite solar cells using passivated tin oxide as an electron transport layer, *Adv. Sci.*, 2018, **5**, 1800130.

11  Q. Jiang, X. Zhang and J. You, SnO$_2$: a wonderful electron transport layer for perovskite solar cells, *Small*, 2018, **14**, 1801154.

12  Y. Ai, W. Liu, C. Shou, J. Yan, N. Li, Z. Yang, W. Song, B. Yan, J. Sheng and J. Ye, SnO$_2$ surface defects tuned by (NH4)2S for high-efficiency perovskite solar cells, *Sol. Energy*, 2019, **194**, 541–547.

13  S. Zhang, H. Si, W. Fan, M. Shi, M. Li, C. Xu, Z. Zhang, Q. Liao, A. Sattar and Z. J. Kang, Graphdiyne: bridging SnO$_2$ and perovskite in planar solar cells, *Angew. Chem., Int. Ed.*, 2020, **59**, 11573–11582.

14  D. Yang, R. Yang, K. Wang, C. Wu, X. Zhu, J. Feng, X. Ren, G. Fang, S. Priya and S. F. Liu, High efficiency planar-type

15  Q. Liu, X. Zhang, C. Li, H. Lu, Z. Weng, Y. Pan, W. Chen, X.-C. Hang, Z. Sun and Y. J. Zhan, Effect of tantalum doping on SnO$_2$ electron transport layer via low temperature process for perovskite solar cells, *Appl. Phys. Lett.*, 2019, **115**, 143903.

16  X. Ren, D. Yang, Z. Yang, J. Feng, X. Zhu, J. Niu, Y. Liu, W. Zhao and S. F. Liu, Solution-processed Nb: SnO$_2$ electron transport layer for efficient planar perovskite solar cells, *ACS Appl. Mater. Interfaces*, 2017, **9**, 2421–2429.

17  J. Ma, G. Yang, M. Qin, X. Zheng, H. Lei, C. Chen, Z. Chen, Y. Guo, X. Zhao and G. J. Fang, MgO nanoparticle modified anode for highly efficient SnO$_2$-based planar perovskite solar cells, *Adv. Sci.*, 2017, **4**, 1700031–1700031.

18  Z. Zhu, Y. Bai, X. Liu, C. Chueh, S. Yang and A. K. Jen, Enhanced efficiency and stability of inverted perovskite solar cells using highly crystalline SnO$_2$ nanocrystals as the robust electron–transporting layer, *Adv. Mater.*, 2016, **28**, 6478–6484.

19  P. Zhu, S. Gu, X. Luo, Y. Gao, S. Li, J. Zhu and H. Tan, Simultaneous contact and grain–boundary passivation in planar perovskite solar cells using SnO$_2$–KCl composite electron transport layer, *Adv. Energy Mater.*, 2020, **10**, 1903083.

20  C. Li, H. Li, Z. N. Zhu, N. Y. Cui, Z. A. Tan and R. S. Yang, Perovskite passivation strategies for efficient and stable solar cells, *Sol. RRL*, 2021, **5**, 2000579.

21  K. Liu, S. Chen, J. Wu, H. Zhang, M. Qin, X. Lu, Y. Tu, Q. Meng and X. J. E. Zhan, Fullerene derivative anchored SnO2 for high-performance perovskite solar cells, *Energy Environ. Sci.*, 2018, **11**, 3463–3471.

22  Y. Dong, W. Li, X. Zhang, Q. Xu, Q. Liu, C. Li and Z. Bo, Highly efficient planar perovskite solar cells via interfacial modification with fullerene derivatives, *Small*, 2016, **12**, 1098–1104.

23  P.L. Qin, T. Wu, Z. C. Wang, X. L. Zheng, X. L. Yu, G. J. Fang and G. Li, Vitrification transformation of poly (ethylene oxide) activating interface passivation for high-efficiency perovskite solar cells, *Sol. RRL*, 2019, **3**, 1900134.

24  W. J. Yin, T. Shi and Y. Yan, Unusual defect physics in CH$_3$NH$_3$PbI$_3$ perovskite solar cell absorber, *Appl. Phys. Lett.*, 2014, **104**, 063903.

25  W. Ke, G. Fang, Q. Liu, L. Xiong, P. Qin, H. Tao, J. Wang, H. Lei, B. Li and J. Wan, Low-temperature solution-processed tin oxide as an alternative electron transporting layer for efficient perovskite solar cells, *J. Am. Chem. Soc.*, 2015, **137**, 6730–6733.

26  P. Zhang, F. Yang, M. A. Kamarudin, C. H. Ng, G. Kapil, T. Ma and S. Hayase, Performance enhancement of mesoporous TiO$_2$-based perovskite solar cells by SbI$_3$ interfacial modification layer, *ACS Appl. Mater. Interfaces*, 2018, **10**, 29630–29637.

27  M. Zhang, F. Wu, D. Chi, K. Shi and S. Huang, High-efficiency perovskite solar cells with poly (vinylpyrroli-

done)-doped SnO$_2$ as an electron transport layer, *Mater. Adv.*, 2020, **1**, 617–624.

28 Q. Guo, F. L. Yuan, B. Zhang, S. J. Zhou, J. Zhang, Y. M. Bai, L. Z. Fan, T. Hayat, A. Alsaedi and Z. A. Tan, Passivation of the grain boundaries of CH$_3$NH$_3$PbI$_3$ using carbon quantum dots for highly efficient perovskite solar cells with excellent environmental stability, *Nanoscale*, 2019, **11**, 115–124.

29 D. Yang, R. Yang, X. Ren, X. Zhu, Z. Yang, C. Li and S. Liu, Hysteresis-suppressed high-efficiency flexible perovskite solar cells using solid-state ionic-liquids for effective electron transport, *Adv. Mater.*, 2016, **28**, 5206–5213.

30 F. Yang, P. Zhang, M. A. Kamarudin, G. Kapil, T. Ma and S. Hayase, Addition effect of pyreneammonium iodide to methylammonium lead halide perovskite-2D/3D heterostructured perovskite with enhanced stability, *Adv. Funct. Mater.*, 2018, **28**, 1804856.

31 H. Su, J. Zhang, Y. Hu, X. Du, Y. Yang, J. You, L. Gao and S. Liu, Fluoroethylamine Engineering for effective passivation to attain 23.4% efficiency perovskite solar cells with superior stability, *Adv. Energy Mater.*, 2021, **23**, 2101454.

32 H. Jiang, X. Qu, L. He, Z. Lv, D. Li, F. Wang, L. Fan, J. Yang, L. Yang and Y. Yan, A design strategy of additive molecule for PSCs: anchoring intrinsic properties of functional groups by suppressing long-range conjugation effect, *J. Energy Chem.*, 2021, 131676.

33 S. Yang, Q. Han, L. Wang, Y. Zhou, F. Yu, C. Li, X. Cai, L. Gao, C. Zhang and T. Ma, Over 23% Power Conversion Efficiency of Planar Perovskite Solar Cells via Bulk Heterojunction Design, *Chem. Eng. J.*, 2021, 131838.

34 X. Li, W. Li, Y. Yang, X. Lai, Q. Su, D. Wu, G. Li, K. Wang, S. Chen and X. W. Sun, Defects passivation with dithienobenzodithiophene–based π–conjugated polymer for enhanced performance of perovskite solar cells, *Sol. RRL*, 2019, **3**, 1900029.

35 Z. Zhu, Y. Bai, H. K. H. Lee, C. Mu, T. Zhang, L. Zhang, J. Wang, H. Yan, S. K. So and S. Yang, Polyfluorene derivatives are high–performance organic hole-transporting materials for inorganic-organic hybrid perovskite solar cells, *Adv. Funct. Mater.*, 2014, **24**, 7357–7365.

36 Y. Yang, J. Wu, X. Wang, Q. Guo, X. Liu, W. Sun, Y. Wei, Y. Huang, Z. Lan and M. Huang, Suppressing vacancy defects and grain boundaries via ostwald ripening for high–performance and stable perovskite solar cells, *Adv. Mater.*, 2020, **32**, 1904347.

37 W. Chen, Y. Wu, Y. Yue, J. Liu, W. Zhang, X. Yang, H. Chen, E. Bi, I. Ashraful and M. Grätzel, Efficient and stable large-area perovskite solar cells with inorganic charge extraction layers, *Science*, 2015, **350**, 944–948.